RSC Advances

PAPER

View Article Online
View Journal | View Issue

Cite this: *RSC Adv.*, 2022, **12**, 13653

A free-standing VN/MXene composite anode for high-performance Li-ion hybrid capacitors†

Zihan Guo,[a] Zhiwei Wang,[ab] Dong Wang,[a] Yanfang Gao *[a] and Jinrong Liu*[a]

Received 24th January 2022
Accepted 22nd April 2022

DOI: 10.1039/d2ra00496h

rsc.li/rsc-advances

The Li-ion hybrid capacitor (LIHC) is considered as a promising candidate for electrochemical energy storage owing to the high energy and power density. However, the sluggish anodic reaction kinetics and high reaction voltage greatly hinder the overall performance of LIHCs. Herein, a free-standing VN/MXene composite anode with high specific capacity and low reaction voltage was prepared by a simple vacuum filtration method. The obtained VN/MXene composite anode shows a high discharge specific capacity of 501.7 mA h g^{-1} at 0.1 A g^{-1} and excellent rate capability (191.8 mA h g^{-1} at 5 A g^{-1}), as well as much extended cycling stability (1500 cycles at 2 A g^{-1}). When combined with an egg white-derived activated carbon (E-AC) cathode, the assembled LIHC delivers a high specific capacity of 59.1 F g^{-1} and a high energy density of 129.3 W h kg^{-1} with a power density of 449.7 W kg^{-1}. Even at a high current density of 5 A g^{-1}, the LIHC still maintains an exciting energy density of 42.81 W h kg^{-1} at 11 249 W kg^{-1}. Meanwhile, the cycling life can be extended to 5000 cycles with a high capacity retention of 98% at 1 A g^{-1}. We believe that this work opens up new possibilities for developing advanced free-standing MXene-based electrodes for Li-ion storage.

Introduction

The Li-ion hybrid capacitor (LIHC) is the most promising electrochemical energy storage device to simultaneously meet the requirements of high energy density and excellent power density.[1–6] Generally, a LIHC is composed of a battery-type anode and a capacitive-type cathode, and the two electrodes are separated by a separator which is infiltrated by the commonly used aprotic electrolyte of Li-ion batteries (LIBs). The battery-type anode undergoes a lithiation and delithiation reaction, and the capacitive-type cathode experiences simple adsorption and desorption of PF_6^- during the charging and discharging process.[7] The capacity and energy density of the device is limited by the capacitive-type cathode due to the surface anion adsorption/desorption mechanism.[8,9] In addition, the sluggish lithiation/delithiation reaction kinetics and the poor cycling stability, as well as the high reaction voltage greatly restrict the overall performance of LIHC.[10–12] Thus, numerous efforts are made to develop novel anodic materials and construct a unique structure to improve the overall performance of LIHCs.[2,13–16]

Among all anode materials, VN offers significant application potential for LIB and supercapacitor due to the excellent electrical conductivity ($\sim 10^6\ \Omega^{-1}\ m^{-1}$), high theoretical specific capacity ($\sim$1043 mA h g^{-1}), unique pseudocapacitive-dominated surface charge storage mechanism and low lithiation potential similar to graphite,[17–19] but its weak rate capability and cycling stability limit the practical application.[20,21] In an early study, Wang *et al.* constructed an VN nanowires/graphene composite through a simple hydrothermal method. The porous VN nanowires/graphene composite showed an enhanced specific capacity and rate performance compared to the VN nanowires.[22] When coupled with a polyaniline-derived activated carbon cathode, the assembled LIHC exhibits an excellent energy density of 162 W h kg^{-1} and a power density of 10 W h kg^{-1}.

In addition, MXenes have received considerable attention due to their excellent electrical conductivity, abundant surface functional groups, and unique two-dimensional layered structure.[23,24] More importantly, $Ti_3C_2T_x$ can form flexible films by filtration of colloidal suspensions, allowing the development of a free-standing electrode.[25,26] However, the use of MXenes for alkali metal ion storage is restricted by the sluggish Li^+ diffusion in the interlayer of MXenes and the serious volume variation due to the narrow interlayer space.[27,28] Generally, numerous strategies are devoted to widening the interlayer space of MXenes through inserting the large cations such as NH_4^+ and La^{3+} into the interlayer space of MXenes or designing some hybrids through coupling MXenes with TiO_2 nanoparticles, SnO_2 quantum dots and carbon nanotubes (CNTs) to boost the performance of MXene-based materials for Li^+ storage.[29–33] In addition, MXene is easy to oxidize, avoiding high temperature

[a]*School of Chemical Engineering, Inner Mongolia University of Technology, Hohhot, 010051, P. R. China. E-mail: yf_gao@imut.edu.cn; liujr@imut.edu.cn*

[b]*Engineering Management Department, Inner Mongolia University of Finance and Economics, Hohhot, 010070, P. R. China*

† Electronic supplementary information (ESI) available. See https://doi.org/10.1039/d2ra00496h

treatment. Especially, Zhang *et al.* demonstrated that the MoO_3 nanobelts/MXene composite by a simple vacuum filtration method could effectively overcome the shortcomings of the sluggish reaction kinetics and the rapid capacity decay of MoO_3 for lithium-ion storage. As a result, this composite delivered an enhanced reversible capacity of 1258 mA h g^{-1}, excellent rate capability and cycling stability due to the synergistic effect of MoO_3 nanobelts and MXene.[34]

Inspired by the above work, we consider that constructing a VN/MXene composite is an efficient strategy to improve the lithium-ion storage performance of VN. In this work, we constructed the VN/MXene composite free-standing electrode by mixing prefabricated VN nanowires and MXene nanosheets in an aqueous solution under ultrasonication, followed by a simple vacuum filtration method. MXene as the conductive substrate and flexible skeleton of VN/MXene free-standing electrode could alleviate the structural destruction of VN during charge and discharge, ensuring excellent cycle stability. VN nanowires act as "spacers" between MXene nanosheets to prevent restacking, so as to increase the layer space, which provides unobstructed channels for electrolyte ions and improves the rate capacity. As expected, benefiting from the integrated merits of the one-dimensional VN nanowires and two-dimensional MXene nanosheets, the resultant VN/MXene composite electrode possesses the enhanced electronic conductivity and improved Li^+ diffusion kinetics due to the formation of a three-dimensional network structure, which greatly improves the lithium-ion storage performance of the VN/MXene composite electrode. This composite electrode delivers a high discharge specific capacity of 501.7 mA h g^{-1} at 0.1 A g^{-1}, and even at 5 A g^{-1}, it still has a high specific capacity of 191.8 mA h g^{-1}. Based on an egg white-derived activated carbon (E-AC) cathode and a VN/MXene anode, the constructed LIHC exhibited an ultrahigh energy density of 129.3 W h kg^{-1} at 449.7 W kg^{-1}, which also remains at 42.81 W h kg^{-1} even at a high power density of 11 249 W kg^{-1}. This work shows promising potential for the development of new electrode materials for constructing advanced LIHCs with high energy density and power density simultaneously.

Experimental section

Synthesis of VN nanowires

The VN nanowires were prepared by a literature method.[35] All chemical regents were purchased from Sigma-Aldrich company. Firstly, 0.8 g V_2O_5 powder was gradually added into the mixed solution composed of 10 mL H_2O_2 (30%) and 50 mL deionized water under vigorous stirring for 2 h. After that, the solution was transferred into a Teflon-lined stainless steel autoclave with a volume of 100 mL. Then, the Teflon-lined autoclave was heated to 230 °C and maintained for 24 h. Afterward, the yellow V_2O_5 hydrogel was obtained after naturally cooling to room temperature, which was soaked 5 times in deionized water. Yellow V_2O_5 aerogel was finally obtained by freeze-drying for three days. After that, the VN powder was obtained after annealing in a tube furnace at 800 °C for 2 h under an NH_3 atmosphere using a heating rate of 2 °C min^{-1}.

Synthesis of MXene nanosheets

The $Ti_3C_2T_x$ nanosheets was prepared by a literature method.[36] 1.0 g Ti_3AlC_2 powders were added into 20 mL concentrated HCl solution with 1.0 g LiF. The suspension was stirred in a sealed container at 35 °C for 24 hours. Then, the black slurry was rinsed with deionized water until the pH of the solution is about 6. After that, the suspension undergoes a sonication treatment for 1 h in an Ar atmosphere. The few-layered MXene dispersion was obtained by centrifugation at 3500 rpm. After removing the residues, the suspension was frozen in liquid nitrogen. Finally, the few-layered MXene nanosheets were obtained by freeze-drying for three days.

Synthesis of VN/MXene composite

The MXene aqueous and the VN nanowires were mixed with a weight ratio of 1 : 4 after ultrasonic treatment for 6 h. The VN/MXene composite film was obtained by a simple vacuum filtration step followed by drying in a vacuum oven under 60 °C overnight. The MXene film was prepared by the same step without the addition of VN nanowires.

Synthesis of E-AC

The E-AC was prepared according to a previous report.[37] 0.5 g of sodium chloride was dissolved into the mixture of 20 mL fresh egg white and 5 mL deionized water. The solution was heated at 100 °C until a protein gel was obtained. After freeze-drying, the xerogel was carbonized in a tube furnace at 700 °C for 2 h in an Ar atmosphere. The NaCl was removed with 1 M HCl solution and the carbonized products were obtained. Finally, the E-AC was obtained by activating the carbonized products with KOH at 700 °C for 2 h and subsequently washing with the deionized water.

Materials characterization

The morphologies of the $Ti_3C_2T_x$ nanosheets, VN nanowires, $Ti_3C_2T_x$ film and VN/MXene composite film were observed by scanning electron microscope (SEM, Hitachi S4800, Japan) and transmission electron microscopy (TEM, JEOL JEM-2100F, Japan). X-ray diffraction (XRD, PANalytical Empyrean, Holland) diffractometer was performed to check the crystal structures of the samples using Cu Ka radiation with a scan rate of 2° min^{-1}.

Electrochemical measurements

The free-standing $Ti_3C_2T_x$ film electrode and VN/MXene composite film electrode were prepared by cutting the disk with a diameter of 14 mm. Li foil with a diameter of 15.6 mm was used as anode and 1 M $LiPF_6$ EC/DEC was used as electrolyte. The coin cells were assembled in Ar-filled glovebox with H_2O and O_2 content below 0.1 ppm. The voltage window of half-battery is 0.01–3.0 V. The cathode for LIHC was prepared by coating the slurry composed of E-AC, Super-P, and PTFE with a weight ratio of 8 : 1 : 1. After drying at 110 °C for 12 h, the E-AC cathode was coupled with a pre-lithiated VN/MXene composite anode to construct LIHC, and 1 M $LiPF_6$ EC/DEC was used as the

electrolyte of LIHC. The working voltage window for the LIHC is 0.5–4.0 V. The specific capacitance (C, F g^{-1}), energy density (E, W h kg^{-1}) and power density (P, W kg^{-1}) were calculated from eqn (1)–(3):

$$C = \frac{I\Delta t}{\Delta V} \quad (1)$$

$$E = \frac{0.5CV^2}{3.6} \quad (2)$$

$$P = \frac{E}{\Delta t} \times 3600 \quad (3)$$

where I is the current density, ΔV is the working voltage window, Δt is the discharging time and m is the total weight of both anode and cathode.

Cyclic voltammetry (CV) curves were obtained on a CHI760E electrochemical station (Shanghai, China). Galvanostatic charge/discharge (GCD) curves of the cells were collected on a Land CT2001A and G340A model battery test system (Wuhan, China).

Results and discussion

Curled $Ti_3C_2T_x$ nanosheets (Fig. 1a) were prepared by etching the Al components of Ti_3AlC_2 with LiF/HCl and a subsequent freeze-drying process. The curled $Ti_3C_2T_x$ nanosheets could easily form the $Ti_3C_2T_x$ nanosheets film by a vacuum filtration step. Owing to the existence of multiple functional groups on the surface of $Ti_3C_2T_x$ nanosheets, the prepared $Ti_3C_2T_x$ nanosheets could be uniformly dispersed in the water to form $Ti_3C_2T_x$ nanosheets ink (Fig. 1b, left). Fig. 1c shows that the curled $Ti_3C_2T_x$ nanosheets are stacked to form compact film, except for a small quantity of curled $Ti_3C_2T_x$ nanosheets that are observed on the surface of the $Ti_3C_2T_x$ film. The VN nanowires were prepared by a simple hydrothermal process and a subsequent ammonifying process. The X-ray diffraction (XRD) pattern (Fig. S1†) indicating that the V_2O_5 have been successfully prepared. Scanning electron microscopy (SEM) result shows that the V_2O_5 powders were transformed into very long V_2O_5 nanowires (Fig. S2†) during the hydrothermal process. After ammonifying treatment, the lattice oxygen atoms of V_2O_5 nanowires were substituted by nitrogen atoms, which results in the morphology change of V_2O_5 nanowires. In spite of that, the as-prepared VN still keeps the one-dimensional structure except for the lower length-diameter ratio compared to V_2O_5 nanowires (Fig. 1d). This is consistent with the previous reports.[38] The transmission electron microscope (TEM) images in Fig. 1e and S3† show the VN nanowires are composed of ultrafine VN nanoparticles with a size of about 2 nm. The magnified TEM image (Fig. 1f) shows that the lattice fringes with the interplanar

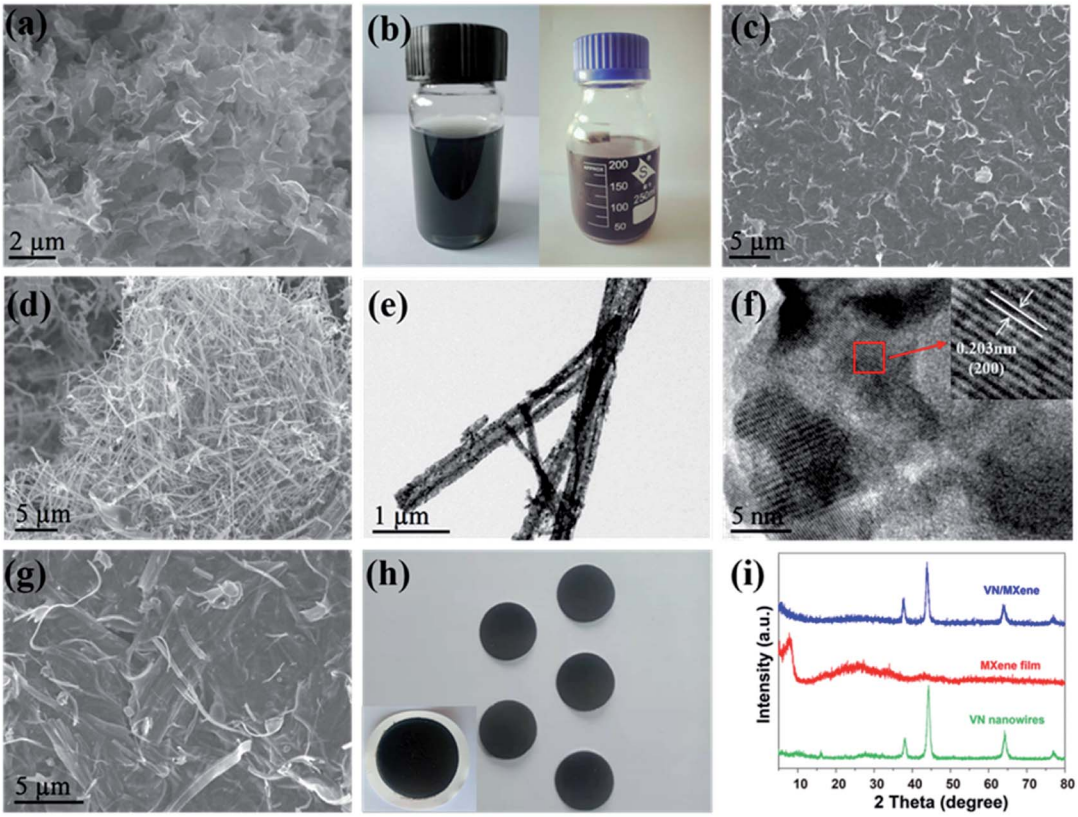

Fig. 1 (a) SEM images of the prepared $Ti_3C_2T_x$ nanosheets. (b) Photographs of $Ti_3C_2T_x$-water dispersion and VN-$Ti_3C_2T_x$-water dispersion. (c) SEM images of the prepared $Ti_3C_2T_x$ film. (d) SEM image of the prepared VN nanowires. (e) TEM and (f) HRTEM images of VN nanowires. (g) SEM images of VN/MXene composite film. (h) Photographs of free-standing VN/MXene composite film electrode. (i) XRD patterns of the $Ti_3C_2T_x$ film, VN nanowires and VN/MXene composite, respectively.

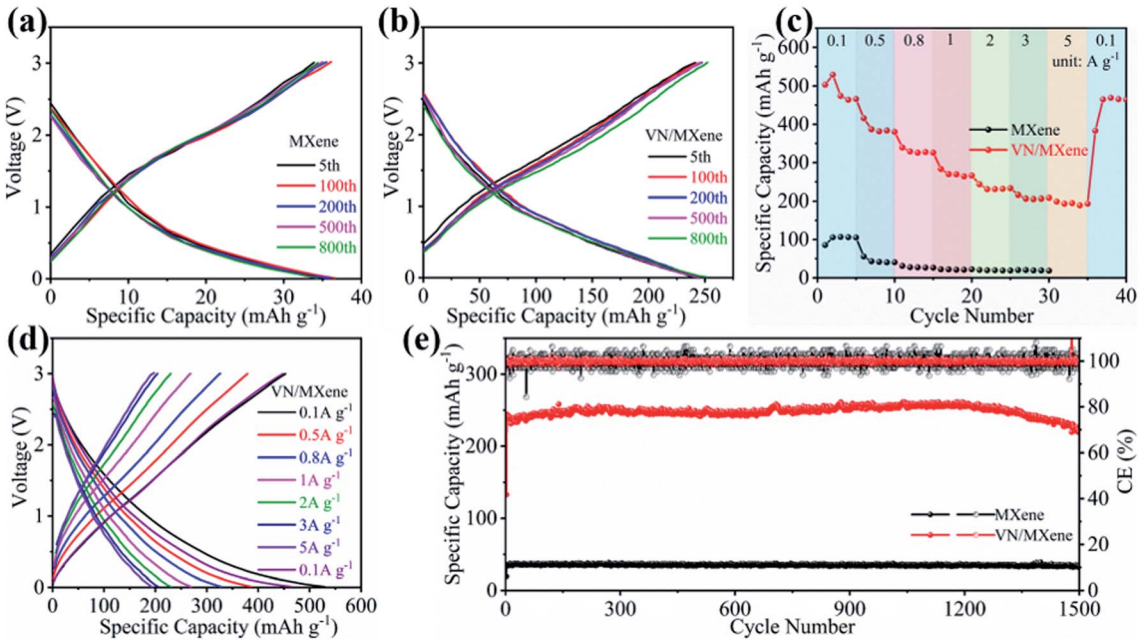

Fig. 2 (a) Charge and discharge curves of MXene film electrode in different cycles. (b) Charge and discharge curves of VN/MXene composite electrode in different cycles. (c) Rate performance of MXene film electrode and VN/MXene composite electrode. (d) Charge and discharge curves of VN/MXene composite electrode at different current densities. (e) Cycling performance of MXene film electrode and VN/MXene composite electrode at 2 A g^{-1}.

spacings of 0.20 nm is corresponding to the (200) facets, which is in line with the results of XRD (JCPDS 78-1315).[35] Such fluffy nanowire coil could form uniform dispersion with curled $Ti_3C_2T_x$ nanosheets in an aqueous medium (Fig. 1b, right). The freestanding VN/MXene composite film was prepared by a simple vacuum filtration. As shown in Fig. 1g, the $Ti_3C_2T_x$ nanosheets and VN nanowires are evenly distributed in the film where the VN nanowires are filled in the layers of $Ti_3C_2T_x$ nanosheets to form a compact film (Fig. 1h, left). Such a compact film can be tailored to the freestanding composite

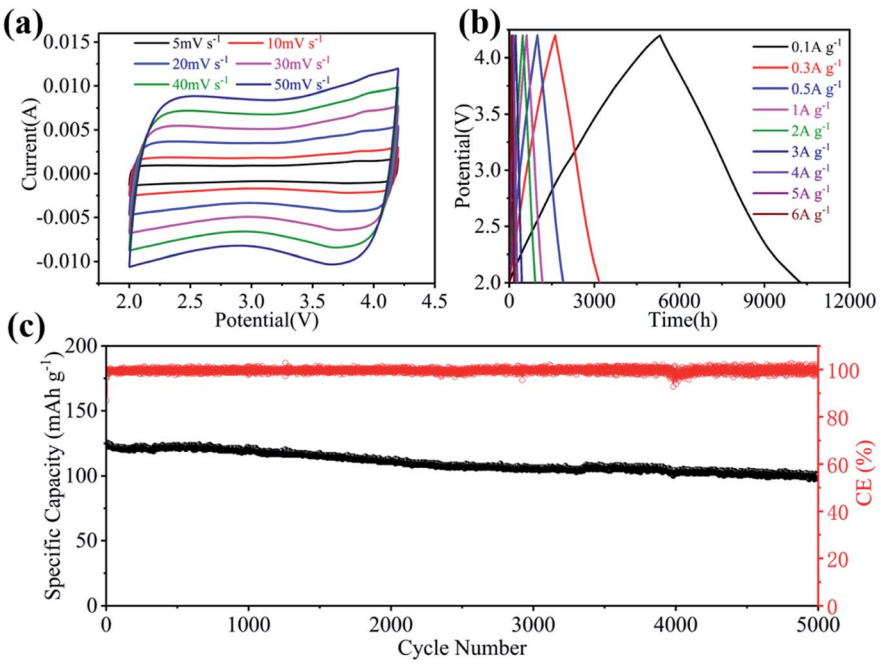

Fig. 3 (a) CV profiles of E-AC at different scan rates in 2.0–4.2 V. (b) GCD profiles of E-AC at various current densities in 2.0–4.2 V. (c) Cycle stability of E-AC at 2 A g^{-1}.

electrode with controlled diameters for Li-ions storage (Fig. 1h, right). X-ray diffraction (XRD) was performed to explore the structure of the VN nanowires, $Ti_3C_2T_x$ nanosheets film, and VN/MXene composite film (Fig. 1i). It is clearly seen that the diffraction peaks at 37.6°, 43.7° and 63.5° are corresponding to the (111), (200), and (220) crystal planes of cubic phase VN (JCPDS 78-1315).[35] From the XRD patterns of film, the existence of a strong peak is corresponding to the (002) crystal plane of $Ti_3C_2T_x$ nanosheets.[39] For VN/MXene composite film, the existence of strong diffraction peaks of VN proves the successful composite of VN nanowires and $Ti_3C_2T_x$ nanosheets. According to the above characterization, we consider that the composite of VN nanowires and $Ti_3C_2T_x$ nanosheets could open the channel for the electrolyte infiltration, and thus to greatly enhanced the performance of $Ti_3C_2T_x$ nanosheets.

The electrochemical performance of $Ti_3C_2T_x$ film and VN/MXene composite film were evaluated in half-battery. The cyclic voltammetry (CV) curve of VN/MXene electrode is shown in Fig. S4.† The two redox peaks at approximately at 1.29 and 0.96 V, which may be attributed to a lithium reversible reaction with VN in the conversion mechanism.[40] Fig. 2a shows the discharge–charge profiles of $Ti_3C_2T_x$ film at various cycles at 2 A g^{-1}. Although the discharge–charge profiles of $Ti_3C_2T_x$ film are almost overlapped after 800 cycles, the $Ti_3C_2T_x$ film exhibits a low reversible capacity of 33.9 mA h g^{-1}. By contrast, the discharge–charge profiles of VN/MXene film have a much improved reversible capacity of 242.2 mA h g^{-1} and an overlapped discharge–charge profiles during 800 cycles (Fig. 2b), indicating the enhanced capacity and cyclability. Fig. 2c, d and S5† present the rate performance of $Ti_3C_2T_x$ film and VN/MXene composite film. The capacity of $Ti_3C_2T_x$ film electrode is 85.5 mA h g^{-1}, and the capacities are rapidly decreased with the increase of current densities. However, the capacities of VN/MXene composite film electrode are 501.7 mA h g^{-1} at 0.1 A g^{-1}, 383.9 mA h g^{-1} at 0.5 A g^{-1}, 323.9 mA h g^{-1} at 0.8 A g^{-1}, 266.7 mA h g^{-1} at 1 A g^{-1}, 230.5 mA h g^{-1} at 2 A g^{-1},

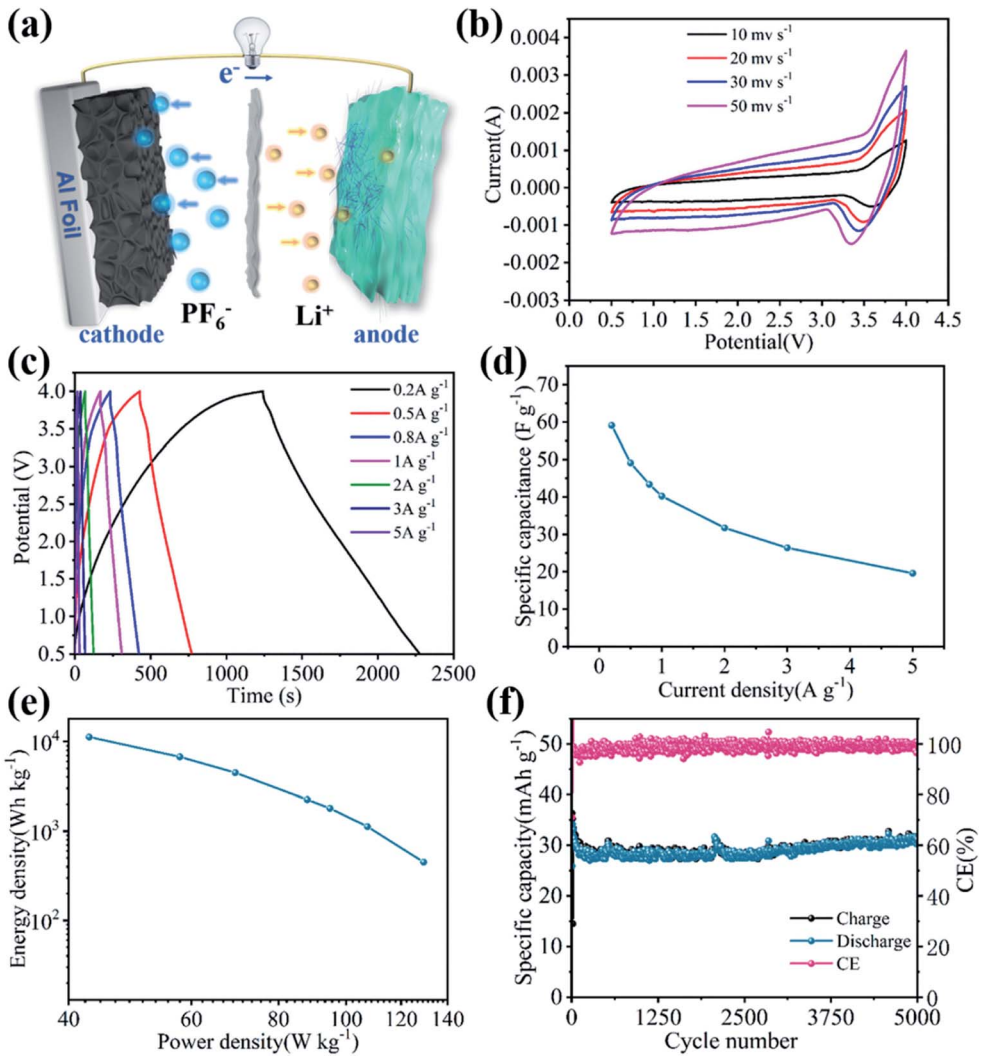

Fig. 4 (a) Schematic illustration of device structure and working mechanism of VN/MXene//E-AC LIHC. (b) CV curves of the VN/MXene//E-AC LIHC at different sweep rates in 0.5–4.0 V. (c) GCD curves of VN/MXene//E-AC LIHC at different current densities in 0.5–4.0 V. (d) Rate performance of VN/MXene//E-AC LIHC. (e) Ragone plots of the VN/MXene//E-AC LIHC. (f) Cycle stability of the VN/MXene//E-AC LHIC at a current density of 1 A g^{-1} in 0.5–4.0 V.

206.2 mA h g^{-1} at 3 A g^{-1}, 191.8 mA h g^{-1} at 5 A g^{-1}, respectively, exhibiting excellent rate capability (Fig. 2c and d). More importantly, the VN/MXene composite film electrode shows excellent cyclability and maintains high specific capacities simultaneously for 1500 cycles at 2 A g^{-1} (Fig. 2e). Therefore, VN/MXene composite film is an excellent anode for high-performance LIB and LIHC.

To construct LIHC, the cathode material was prepared by using egg white as a precursor, and the prepared activated carbon is named E-AC. The electrochemical performance of capacitive E-AC cathode was tested in a half-cell configuration, where Li foil was used as anode and E-AC was used as cathode. Fig. 3a shows the cyclic voltammetry (CV) curves of E-AC cathode at various scanning rates from 5 mV s^{-1} to 50 mV s^{-1} in 2.0–4.2 V *vs.* Li^+/Li. In the overall scanning rate range, the quasi rectangular-like CV curves are retained, indicating the dominant electronic double-layer capacitor (EDLC) behavior and the excellent rate performance of E-AC. The galvanostatic charge/discharge tests (GCD) were performed at different current densities. As shown in Fig. 3b, isosceles triangle-like GCD curves are obtained and no obvious voltage platforms are observed, representing the main capacity contribution of the ion adsorption/desorption mechanism, which is in an accordance with the CV results. Fig. 3c gives the cyclic performance of the E-AC cathode at 2 A g^{-1}. It reveals that the E-AC cathode shows a specific capacity of 123.9 mA h g^{-1} and the long-term stability for over 5000 cycles with a capacity retention of 81%. These results prove that E-AC is a very promising capacitive cathode for LIHC.

LIHC was assembled with the as-prepared VN/MXene composite film anode and E-AC cathode. Fig. 4a presents the device structure and working mechanism of LIHC based on the VN/MXene composite anode and the E-AC cathode. During the charging/discharging process, the Li ions occur an electrochemical intercalation/deintercalation in VN/MXene composite, and the PF_6^- anions are electrochemically absorbed/desorbed on the surface of the porous structure of the E-AC cathode. To extend the working potential window and balance the charge between VN/MXene anode and E-AC cathode, a pre-lithiation procedure for VN/MXene anode and a mass match for cathode and anode were performed before the fabrication of the device. As shown in Fig. 4b, the CV curves of VN/MXene//E-AC present some slight deviation from the ideal rectangle shape due to the integration of battery-type VN/MXene anode and capacitive E-AC cathode in the voltage range of 0.5–4.0 V. With the increase of sweep rate, the CV curves still maintain the near rectangular shape, exhibiting good reversibility and excellent rate capability. Fig. 4c presents the discharge and charge curves of the VN/MXene//E-AC at various current densities, where the near-linear isosceles triangles with no voltage drop were observed. The specific capacitances of VN/MXene//E-AC based on VN/MXene composite anode and E-AC cathode are 59.1, 49.1, 43.4, 40.2, 31.7, 26.4, and 19.6 F g^{-1} at the current densities of 0.2, 0.5, 0.8, 1, 2, 3, and 5 A g^{-1}, respectively. Benefiting from the integrated advantage of VN/MXene composite anode and E-AC cathode, the VN/MXene//E-AC exhibits a much enhanced rate capability (Fig. 4d). According to the discharge and charge curves, the energy density values and the power density values of the VN/MXene//E-AC LHIC are plotted in Fig. 4e. It should be noted that the VN/MXene//E-AC LHIC can achieve a maximal energy density of 129.3 W h kg^{-1} at a power density of 449.7 W kg^{-1}. When the current density is increased to 5 A g^{-1}, VN/MXene//E-AC LHIC still retains a high energy density of 42.81 W h kg^{-1} and simultaneously achieves an excellent power density of 11 249 W kg^{-1}. Furthermore, the cycling performance of VN/MXene//E-AC LHIC was tested to evaluate the practical applications (Fig. 4f). As expected, a superior cycling life-span with a specific capacity of 31 mA h g^{-1} was obtained at 1 A g^{-1}, accompanied by an outstanding capacity retention of 98.3% after ultra-long cycling for 5000 cycles.

Conclusions

In summary, a free-standing VN/MXene composite anode with high specific capacity and low reaction voltage was prepared by a simple vacuum filtration method. Such a composite electrode integrating the individual merits of $Ti_3C_2T_x$ nanosheets and VN nanowires, thus greatly enhanced the Li-ion storage performance compared to the $Ti_3C_2T_x$ nanosheets. As a result, the VN/MXene composite anode shows a much enhanced specific capacity of 501.7 mA h g^{-1} at 0.1 A g^{-1}, excellent rate performance of 191.8 mA h g^{-1} at 5 A g^{-1} and an improved cycling life for 1500 cycles at 2 A g^{-1}, which is a very promising anode for the application in LIHCs and LIBs. Furthermore, a capacitive E-AC cathodic material was prepared by carbonization and activation of egg white. The as-prepared E-AC shows excellent ions adsorption/desorption mechanism, which leads to remarkable capacity, rate capability and cycling stability. The constructed LIHC based on such a VN/MXene composite anode and E-AC cathode can deliver a high specific capacity of 59.1 F g^{-1}, the maximum energy of 129.3 W h kg^{-1}, and a power density of 11 249 W kg^{-1} in the working voltage range of 0.5–4.0 V. Furthermore, the LIHC shows a super-long cycling life for 5000 cycles with a capacity retention of 98% at 1 A g^{-1}. This work provides a very promising strategy for the development of a novel composite anode for designing advanced LIBs and LIHCs with excellent energy density and power density.

Author contributions

Y. G. and J. L. designed the concept; D. W. and Z. W. provided helpful advice during the writing process; Z. G. performed the experiments and wrote the manuscript. All authors have read and agreed to the published version of the manuscript.

Conflicts of interest

There are no conflicts to declare.

Acknowledgements

This work was supported by National Natural Science Foundation of China (No. 21566030) and Inner Mongolia Autonomous Region Key Technology Research Projects (No. 2020GG0290).

References

1 H. Wang, C. Zhu, D. Chao, Q. Yan and H. J. Fan, *Adv. Mater.*, 2017, **29**, 1702093.
2 V. Aravindan, J. Gnanaraj, Y.-S. Lee and S. Madhavi, *Chem. Rev.*, 2014, **114**, 11619–11635.
3 J. Ding, W. Hu, E. Paek and D. Mitlin, *Chem. Rev.*, 2018, **118**, 6457–6498.
4 C. Han, H. Li, R. Shi, L. Xu, J. Li, F. Kang and B. Li, *Energy Environ. Mater.*, 2018, **1**, 75–87.
5 Y. Ma, H. Chang, M. Zhang and Y. Chen, *Adv. Mater.*, 2015, **27**, 5296–5308.
6 H. Jiang, H. Zhang, L. Chen, Y. Hu and C. Li, *Small*, 2020, **16**, 2002351.
7 M. Yang, Y. Zhong, J. Ren, X. Zhou, J. Wei and Z. Zhou, *Adv. Funct. Mater.*, 2015, **5**, 1500550.
8 H. Jiang, P. S. Lee and C. Li, *Energy Environ. Sci.*, 2013, **6**, 41–53.
9 B. Liu, J. Chen, B. Yang, L. Liu, Y. Sun, R. Hou, Z. Lin and X. Yan, *J. Mater. Chem. A*, 2021, **9**, 10722–10730.
10 X. Wang, L. Liu and Z. Niu, *Mater. Chem. Front.*, 2019, **3**, 1265–1279.
11 H. Kim, M. Y. Cho, M. H. Kim, K. Y. Park, H. Gwon, Y. Lee, K. C. Roh and K. Kang, *Adv. Energy Mater.*, 2013, **3**, 1500–1506.
12 G. Wang, C. Lu, X. Zhang, B. Wan, H. Liu, M. Xia, H. Gou, G. Xin, J. Lian and Y. Zhang, *Nano Energy*, 2017, **36**, 46–57.
13 C. Zhang, H. Song, C. Liu, Y. Liu, C. Zhang, X. Nan and G. Cao, *Adv. Funct. Mater.*, 2015, **25**, 3497–3504.
14 Q. Xia, H. Yang, M. Wang, M. Yang, Q. Guo, L. Wan, H. Xia and Y. Yu, *Adv. Energy Mater.*, 2017, **7**, 1701336.
15 X. Zhao, H.-E. Wang, J. Cao, W. Cai and J. Sui, *Chem. Commun.*, 2017, **53**, 10723–10726.
16 T. Yuan, S. Luo, L. Soule, J.-H. Wang, Y. Wang, D. Sun, B. Zhao, W. Li, J. Yang and S. Zheng, *Mater. Today*, 2021, **45**, 8–19.
17 D. Choi, G. E. Blomgren and P. N. Kumta, *Adv. Mater.*, 2006, **18**, 1178–1182.
18 X. Xiao, X. Peng, H. Jin, T. Li, C. Zhang, B. Gao, B. Hu, K. Huo and J. Zhou, *Adv. Mater.*, 2013, **25**, 5091–5097.
19 W. Bi, Z. Hu, X. Li, C. Wu, J. Wu, Y. Wu and Y. Xie, *Nano Res.*, 2015, **8**, 193–200.
20 Y. Peng, M. Yu, L. Zhao, X. Ji, T. He, Y. Liu, Q. Wang and F. Ran, *Chem. Eng. J.*, 2021, **417**, 129267.
21 C. Tang, H. Tao, X. Liu and X. Yang, *Energy Fuels*, 2022, **36**, 1043–1051.
22 R. Wang, J. Lang, P. Zhang, Z. Lin and X. Yan, *Adv. Funct. Mater.*, 2015, **25**, 2270–2278.
23 M. Q. Zhao, X. Xie, C. E. Ren, T. Makaryan, B. Anasori, G. Wang and Y. Gogotsi, *Adv. Mater.*, 2017, **29**, 1702410.
24 N. Chen, W. Yang and C. Zhang, *Sci. Technol. Adv. Mater.*, 2021, **22**, 917–930.
25 Z. Wu, X. Liu, T. Shang, Y. Deng, N. Wang, X. Dong, J. Zhao, D. Chen, Y. Tao and Q. H. Yang, *Adv. Funct. Mater.*, 2021, **31**, 2102874.
26 J. Yan, C. E. Ren, K. Maleski, C. B. Hatter, B. Anasori, P. Urbankowski, A. Sarycheva and Y. Gogotsi, *Adv. Funct. Mater.*, 2017, **27**, 1701264.
27 Q. Zhao, Q. Zhu, J. Miao, P. Zhang, P. Wan, L. He and B. Xu, *Small*, 2019, **15**, 1970276.
28 K. Li, M. Liang, H. Wang, X. Wang, Y. Huang, J. Coelho, S. Pinilla, Y. Zhang, F. Qi and V. Nicolosi, *Adv. Funct. Mater.*, 2020, **30**, 2000842.
29 M. R. Lukatskaya, O. Mashtalir, C. E. Ren, Y. Dall'Agnese, P. Rozier, P. L. Taberna, M. Naguib, P. Simon, M. W. Barsoum and Y. Gogotsi, *Science*, 2013, **341**, 1502–1505.
30 Y. Zhang, Z. Yang, B. Zhang, J. Li, C. Lu, L. Kong and M. Liu, *J. Alloys Compd.*, 2020, **835**, 155343.
31 L. Li, G. Jiang, C. An, Z. Xie, Y. Wang, L. Jiao and H. Yuan, *Nanoscale*, 2020, **12**, 10369–10379.
32 H. Liu, X. Zhang, Y. Zhu, B. Cao, Q. Zhu, P. Zhang, B. Xu, F. Wu and R. Chen, *Nano-Micro Lett.*, 2019, **11**, 1–12.
33 K. Ma, H. Jiang, Y. Hu and C. Li, *Adv. Funct. Mater.*, 2018, **28**, 1804306.
34 Y. Zhang, P. Chen, Q. Wang, Q. Wang, K. Zhu, K. Ye, G. Wang, D. Cao, J. Yan and Q. Zhang, *Adv. Energy Mater.*, 2021, **11**, 2101712.
35 J. He and A. Manthiram, *Adv. Energy Mater.*, 2020, **10**, 1903241.
36 C. Zhang, M. P. Kremer, A. Seral-Ascaso, S. H. Park, N. McEvoy, B. Anasori, Y. Gogotsi and V. Nicolosi, *Adv. Funct. Mater.*, 2018, **28**, 1705506.
37 R. Shi, C. Han, H. Li, L. Xu, T. Zhang, J. Li, Z. Lin, C.-P. Wong, F. Kang and B. Li, *J. Mater. Chem. A*, 2018, **6**, 17057–17066.
38 Z. Hou, K. Guo, H. Li and T. Zhai, *CrystEngComm*, 2016, **18**, 3040–3047.
39 K. Rasool, M. Helal, A. Ali, C. E. Ren, Y. Gogotsi and K. A. Mahmoud, *ACS Nano*, 2016, **10**, 3674–3684.
40 C. Li, L. Zhu, S. Qi, W. Ge, W. Ma, Y. Zhao, R. Huang, L. Xu and Y. Qian, *ACS Appl. Mater. Interfaces*, 2020, **12**, 49607–49616.